


Advances in Global Change Research 67

Vincenzo Levizzani
Christopher Kidd · Dalia B. Kirschbaum
Christian D. Kummerow · Kenji Nakamura
F. Joseph Turk *Editors*

A satellite in orbit over Earth, showing the planet's curvature and clouds. The satellite has a large solar panel and a dish antenna.

Satellite Precipitation Measurement

Volume 1

 Springer

Advances in Global Change Research

Volume 67

Series Editor

Markus Stoffel, Institute of Geological Sciences, University of Geneva, Geneva, Switzerland

Advisory Editors

Wolfgang Cramer, IMEP, Bâtiment Villemin, Europole de l'Arbois, Aix-en-Provence, France

Urs Luterbacher, University of Geneva, Geneva, Switzerland

F. Toth, International Institute for Applied Systems Analysis (IIASA), Laxanburg, Austria

More information about this series at <http://www.springer.com/series/5588>

Vincenzo Levizzani • Christopher Kidd
Dalia B. Kirschbaum • Christian D. Kummerow
Kenji Nakamura • F. Joseph Turk
Editors

Satellite Precipitation Measurement

Volume 1

 Springer

Editors

Vincenzo Levizzani
CNR-ISAC
Bologna, Italy

Dalia B. Kirschbaum
Code 617
NASA Goddard Space Flight Center
Greenbelt, MD, USA

Kenji Nakamura
Department of Economics on
Sustainability
Dokkyo University
Saitama, Japan

Christopher Kidd
Earth System Science Interdisciplinary Center
University of Maryland and NASA Goddard
Space Flight Center
Greenbelt, MD, USA

Christian D. Kummerow
Department of Atmospheric Science
Colorado State University
Fort Collins, CO, USA

F. Joseph Turk
Jet Propulsion Laboratory
California Institute of Technology
Pasadena, CA, USA

ISSN 1574-0919

ISSN 2215-1621 (electronic)

Advances in Global Change Research

ISBN 978-3-030-24567-2

ISBN 978-3-030-24568-9 (eBook)

<https://doi.org/10.1007/978-3-030-24568-9>

© Springer Nature Switzerland AG 2020, corrected publication 2022

Chapter 22 is licensed under the terms of the Creative Commons Attribution 4.0 International License (<http://creativecommons.org/licenses/by/4.0/>). For further details see licence information in the chapter.

This work is subject to copyright. All rights are reserved by the Publisher, whether the whole or part of the material is concerned, specifically the rights of translation, reprinting, reuse of illustrations, recitation, broadcasting, reproduction on microfilms or in any other physical way, and transmission or information storage and retrieval, electronic adaptation, computer software, or by similar or dissimilar methodology now known or hereafter developed.

The use of general descriptive names, registered names, trademarks, service marks, etc. in this publication does not imply, even in the absence of a specific statement, that such names are exempt from the relevant protective laws and regulations and therefore free for general use.

The publisher, the authors, and the editors are safe to assume that the advice and information in this book are believed to be true and accurate at the date of publication. Neither the publisher nor the authors or the editors give a warranty, expressed or implied, with respect to the material contained herein or for any errors or omissions that may have been made. The publisher remains neutral with regard to jurisdictional claims in published maps and institutional affiliations.

Cover illustration: Courtesy of NASA

This Springer imprint is published by the registered company Springer Nature Switzerland AG.
The registered company address is: Gewerbestrasse 11, 6330 Cham, Switzerland

*Sognatore è un uomo con i piedi fortemente
appoggiati sulle nuvole**

Ennio Flaiano (1910–1972)

**Dreamer is a man with his feet firmly resting
on the clouds*

In memory of
Arthur Y. Hou (1947–2013)

Preface

This book is published 13 years after the book *Measuring Precipitation from Space: EURAINSAT and the Future* (V. Levizzani, P. Bauer, and F. J. Turk, Eds., Springer, ISBN 978-1-4020-5835-6), but it is not a revised edition of the previous. It is a new book that aims to construct a quasi-complete picture of the science and applications of satellite-derived precipitation measurements at the present time.

The book comes out at the end of a very exciting era of precipitation measurements from space. The Tropical Rainfall Measuring Mission (TRMM), launched in November 1997, ended its long life in space in April 2015 providing an unprecedented 17-year-long dataset of tropical precipitation and lightning. The Global Precipitation Measurement (GPM) mission, launched in February 2014, is now in space as TRMM's natural successor with a more global perspective that extends precipitation radar observations to the Arctic and Antarctic circles. At the same time, the CloudSat mission, launched in April 2006, is in its 13th year in space and focuses on cloud structure, which is essential for improving precipitation retrievals. These are just a few examples of precipitation-oriented missions that continuously provide data from geostationary and low Earth orbits in a truly cooperative effort worldwide. This effort involves many agencies and a broad range of countries who collaborate in a genuine way to observe global precipitation.

It is by realizing the significance of this historical moment and the need to think about what is important for the future that the community joined in the effort of writing a book with the goal of serving the precipitation community itself, the scholars, the students, the stakeholders, the end users, and all the readers interested in knowing the progress of satellite precipitation studies. The most recent achievements in precipitation monitoring from space drive us into the future of measuring not only heavy rainfall but less intense rainfall, snowfall, and even hailfall. Such a scientific framework would not have even been conceivable 13 years ago and is only possible thanks to the relentless effort of the worldwide space and precipitation communities.

Naturally, we realize that at the time of the printing of this book, the field will already have made advances and thus part of the material may already be a bit

outdated. However, in this era of rapidly evolving technological developments, sensors that take years to design, build, and launch are already considered old. This is particularly true nowadays when the progress in approaching new scientific challenges is particularly fast.

Since 2007, science has made substantial progresses toward transforming satellite rainfall “estimates” into accurate “measurements” and producing operational rainfall products readily available for a wide field of applications ranging from climate research and numerical weather prediction to hydrology, agriculture, health, civil protection, and much more. Satellite-derived precipitation products are now being considered as a valuable tool for a number of applications that benefit society and save lives. This is perhaps the most important achievement of all.

This book represents a significant effort, and each author has provided high-quality material in the topics of current and future mission contributions, observations of precipitation using the suite of precipitation satellites, retrieval techniques, validation, and applications. The result is a book that not only photographs the state of the art of the discipline but also projects it into the future.

Bologna, Italy
Greenbelt, MD, USA
Greenbelt, MD, USA
Fort Collins, CO, USA
Saitama, Japan
Pasadena, CA, USA
9 March 2020

Vincenzo Levizzani
Christopher Kidd
Dalia B. Kirschbaum
Christian D. Kummerow
Kenji Nakamura
F. Joseph Turk

Acknowledgments

The first acknowledgment goes to Springer Nature for asking us to start this project and for being very patient with us for the considerable amount of time it took to put the material together.

All the colleagues who spent their precious time contributing their ideas and results deserve special gratitude. They are all very busy scientists, and this is why their contribution is particularly valuable. We deem the book to be a first-hand image of the achievements of the whole community at this time while also providing an important glimpse into future developments.

Then we feel that we need to thank the readers who have already made the previous 2007 Springer book a success, thus de facto making it possible to start writing the new one. We hope you will get from this new book even more inspiration than you got from its predecessor. While some concepts and details will surely become outdated as time goes by, it is our hope that the material contained herein is sufficiently broad that it will always serve as a springboard to understand and put into context the latest research and findings.

It would be almost impossible to thank all the people and organizations behind this effort. You realize this simple truth by looking at the list of contributors and seeing the very long list of institutes, research organizations, university departments, and operational agencies that allowed their members to spend a substantial amount of time writing and correcting the chapters of the book. We thank, in particular, our home institutions that were very supportive in understanding the importance of our work for the community: CNR, Colorado State University, Dokkyo University, JPL-Caltech, NASA, and University of Maryland.

It is very important to remember all the colleagues who are no longer with us and who worked very hard until the last minute providing an essential contribution. This book is dedicated to the memory of a friend of all of us, Arthur Y. Hou (1947–2013). Arthur was not only the US Project Scientist of the Global Precipitation Measurement (GPM) mission, he was a man of a truly global vision who now is in place with the GPM constellation. More than that, he made great efforts to establish an international science cooperation through his gentle and unique way of approaching

each one of us. Other colleagues left us in recent times, and we want to honor them as well: David (Dave) H. Staelin (1938–2011), David I. F. Grimes (1951–2011), and James (Jim) A. Weinman (1930–2012). They all left us much too soon, and we miss them, but their work is here to testify to their essential contribution to the advancement of science and to meet the needs of mankind.

Two major international organizations gave us the opportunity to work together with a global strategy for the future: the International Precipitation Working Group (IPWG) and the World Meteorological Organization (WMO).

The senior editor (Vincenzo Levizzani) would like to recognize the ceaseless work of his coeditors in effectively putting together the material of their respective sections: F. Joseph (Joe) Turk for Section 1, Christian (Chris) D. Kummerow for Sections 2 and 3, Christopher (Chris) Kidd for Section 4, Kenji Nakamura for Section 5, and Dalia B. Kirschbaum for Section 6. Their commitment and competence largely influenced the quality level of this book.

Finally, our families are part of the project through their understanding and their moral and practical support. Without them, the writing of this book would have never even started.

Bologna, Italy
 Greenbelt, MD, USA
 Greenbelt, MD, USA
 Fort Collins, CO, USA
 Saitama, Japan
 Pasadena, CA, USA
 9 March 2020

Vincenzo Levizzani
 Christopher Kidd
 Dalia B. Kirschbaum
 Christian D. Kummerow
 Kenji Nakamura
 F. Joseph Turk

Contents of Volume 1

Part I Status of Observations and Satellite Programs

| | | |
|----------|--|-----------|
| 1 | The Global Precipitation Measurement (GPM) Mission | 3 |
| | Christopher Kidd, Yukari N. Takayabu, Gail M. Skofronick-Jackson, George J. Huffman, Scott A. Braun, Takuji Kubota, and F. Joseph Turk | |
| 2 | Status of the CloudSat Mission | 25 |
| | Matthew D. Lebsock, Tristan S. L’Ecuyer, Norman B. Wood, John M. Haynes, and Mark A. Smalley | |
| 3 | The Megha-Tropiques Mission After Seven Years in Space | 45 |
| | Rémy Roca, Michel Dejus, Philippe Chambon, Sophie Cloché, and Michel Capderou | |
| 4 | Microwave Sensors, Imagers and Sounders | 63 |
| | Kazumasa Aonashi and Ralph R. Ferraro | |
| 5 | Microwave and Sub-mm Wave Sensors: A European Perspective | 83 |
| | Christophe Accadia, Vinia Mattioli, Paolo Colucci, Peter Schlüssel, Salvatore D’Addio, Ulf Klein, Tobias Wehr, and Craig Donlon | |
| 6 | Plans for Future Missions | 99 |
| | Christian D. Kummerow, Simone Tanelli, Nobuhiro Takahashi, Kinji Furukawa, Marian Klein, and Vincenzo Levizzani | |

Part II Retrieval Techniques, Algorithms and Sensors

| | | |
|----------|--|------------|
| 7 | Introduction to Passive Microwave Retrieval Methods | 123 |
| | Christian D. Kummerow | |

8 The Goddard Profiling (GPROF) Precipitation Retrieval Algorithm141
 David L. Randel, Christian D. Kummerow, and Sarah Ringerud

9 Precipitation Estimation from the Microwave Integrated Retrieval System (MiRS)153
 Christopher Grassotti, Shuyan Liu, Quanhua Liu, Sid-Ahmed Boukabara, Kevin Garrett, Flavio Iturbide-Sanchez, and Ryan Honeyager

10 Introduction to Radar Rain Retrieval Methods169
 Toshio Iguchi and Ziad S. Haddad

11 Dual-Frequency Precipitation Radar (DPR) on the Global Precipitation Measurement (GPM) Mission’s Core Observatory183
 Toshio Iguchi

12 DPR Dual-Frequency Precipitation Classification193
 V. Chandrasekar and Minda Le

13 Triple-Frequency Radar Retrievals 211
 Alessandro Battaglia, Simone Tanelli, Frederic Tridon, Stefan Kneifel, Jussi Leinonen, and Pavlos Kollias

14 Precipitation Retrievals from Satellite Combined Radar and Radiometer Observations 231
 Mircea Greu and William S. Olson

15 Scattering of Hydrometeors 249
 Stefan Kneifel, Jussi Leinonen, Jani Tyynelä, Davide Ori, and Alessandro Battaglia

16 Radar Snowfall Measurement 277
 Guosheng Liu

17 A 1DVAR-Based Snowfall Rate Algorithm for Passive Microwave Radiometers 297
 Huan Meng, Cezar Kongoli, and Ralph R. Ferraro

18 X-Band Synthetic Aperture Radar Methods 315
 Saverio Mori, Frank S. Marzano, and Nazzareno Pierdicca

Part III Merged Precipitation Products

19 Integrated Multi-satellite Retrievals for the Global Precipitation Measurement (GPM) Mission (IMERG) 343
 George J. Huffman, David T. Bolvin, Dan Braithwaite, Kuo-Lin Hsu, Robert J. Joyce, Christopher Kidd, Eric J. Nelkin, Soroosh Sorooshian, Erich F. Stocker, Jackson Tan, David B. Wolff, and Pingping Xie

20 Global Satellite Mapping of Precipitation (GSMaP) Products in the GPM Era 355
 Takuji Kubota, Kazumasa Aonashi, Tomoo Ushio, Shoichi Shige, Yukari N. Takayabu, Misako Kachi, Yoriko Arai, Tomoko Tashima, Takeshi Masaki, Nozomi Kawamoto, Tomoaki Mega, Munehisa K. Yamamoto, Atsushi Hamada, Moeka Yamaji, Guosheng Liu, and Riko Oki

21 Improving PERSIANN-CCS Using Passive Microwave Rainfall Estimation 375
 Kuo-Lin Hsu, Negar Karbalee, and Dan Braithwaite

22 TAMSAT 393
 Ross Maidment, Emily Black, Helen Greatrex, and Matthew Young

23 Algorithm and Data Improvements for Version 2.1 of the Climate Hazards Center’s InfraRed Precipitation with Stations Data Set 409
 Chris Funk, Pete Peterson, Martin Landsfeld, Frank Davenport, Andreas Becker, Udo Schneider, Diego Pedreros, Amy McNally, Kristi Arsenault, Laura Harrison, and Shraddhanand Shukla

24 Merging the Infrared Fleet and the Microwave Constellation for Tropical Hydrometeorology (TAPEER) and Global Climate Monitoring (GIRAFE) Applications 429
 Rémy Roca, Adrien Guérou, Rômulo A. Jucá Oliveira, Philippe Chambon, Marielle Gosset, Sophie Cloché, and Marc Schröder

Correction to: TAMSAT C1

Contents of Volume 2

Part IV Validation

| | | |
|-----------|---|------------|
| 25 | The IPWG Satellite Precipitation Validation Effort | 453 |
| | Christopher Kidd, Shoichi Shige, Daniel Vila, Elena Tarnavsky, Munehisa K. Yamamoto, Viviana Maggioni, and Bathobile Maseko | |
| 26 | The GPM Ground Validation Program | 471 |
| | Walter A. Petersen, Pierre-Emmanuel Kirstetter, Jianxin Wang, David B. Wolff, and Ali Tokay | |
| 27 | The GPM DPR Validation Program | 503 |
| | Riko Oki, Toshio Iguchi, and Kenji Nakamura | |
| 28 | Error and Uncertainty Characterization | 515 |
| | Christian Massari and Viviana Maggioni | |
| 29 | Multiscale Evaluation of Satellite Precipitation Products: Effective Resolution of IMERG | 533 |
| | Clément Guilloteau and Efi Foufoula-Georgiou | |
| 30 | Remote Sensing of Orographic Precipitation | 559 |
| | Ana P. Barros and Malarvizhi Arulraj | |
| 31 | Integrated Multi-satellite Evaluation for the Global Precipitation Measurement: Impact of Precipitation Types on Spaceborne Precipitation Estimation | 583 |
| | Pierre-Emmanuel Kirstetter, Walter A. Petersen, Christian D. Kummerow, and David B. Wolff | |
| 32 | Hydrologic Validation and Flood Analysis | 609 |
| | Witold F. Krajewski, Felipe Quintero, Mohamed El Saadani, and Radoslaw Goska | |

33 Global-Scale Evaluation of 22 Precipitation Datasets Using Gauge Observations and Hydrological Modeling 625
 Hylke E. Beck, Noemi Vergopolan, Ming Pan, Vincenzo Levizzani, Albert I. J. M. van Dijk, Graham P. Weedon, Luca Brocca, Florian Pappenberger, George J. Huffman, and Eric F. Wood

34 OceanRAIN – The Global Ocean Surface-Reference Dataset for Characterization, Validation and Evaluation of the Water Cycle 655
 Christian Klepp, Paul A. Kucera, Jörg Burdanowitz, and Alain Protat

Part V Observed Characteristics of Precipitation

35 GPCP and the Global Characteristics of Precipitation 677
 Robert F. Adler, Guojun Gu, George J. Huffman, Mathew R. P. Sapiano, and Jian-Jian Wang

36 Global Snowfall Detection and Measurement 699
 Mark S. Kulie, Lisa Milani, Norman B. Wood, and Tristan S. L’Ecuyer

37 Snowfall Detection by Spaceborne Radars 717
 Atsushi Hamada, Toshio Iguchi, and Yukari N. Takayabu

38 On the Duration and Life Cycle of Precipitation Systems in the Tropics 729
 Rémy Roca, Dominique Bouniol, and Thomas Fiolleau

39 Observational Characteristics of Warm-Type Heavy Rainfall 745
 Byung-Ju Sohn, Geun-Hyeok Ryu, and Hwan-Jin Song

40 Satellite Precipitation Measurement and Extreme Rainfall 761
 Olivier P. Prat and Brian R. Nelson

41 Rainfall Trends in East Africa from an Ensemble of IR-Based Satellite Products 791
 Elsa Cattani, Andrés Merino, and Vincenzo Levizzani

42 Heavy Precipitation Systems in the Mediterranean Area: The Role of GPM 819
 Giulia Panegrossi, Anna Cinzia Marra, Paolo Sanò, Luca Baldini, Daniele Casella, and Federico Porcù

43 Dryland Precipitation Climatology from Satellite Observations 843
 Efrat Morin, Francesco Marra, and Moshe Armon

44 Hailfall Detection 861
 Ralph R. Ferraro, Daniel Cecil, and Sante Laviola

45 Improving High-Latitude and Cold Region Precipitation Analysis 881
 Ali Behrangi

46 Latent Heating Retrievals from Satellite Observations 897
 Yukari N. Takayabu and Wei-Kuo Tao

Part VI Applications

47 Operational Applications of Global Precipitation Measurement Observations 919
 Anita LeRoy, Emily Berndt, Andrew Molthan, Bradley Zavadsky, Matthew Smith, Frank LaFontaine, Kevin McGrath, and Kevin Fuell

48 Assimilation of Precipitation Observations from Space into Numerical Weather Prediction (NWP) 941
 Sid-Ahmed Boukabara, Erin Jones, Alan Geer, Masahiro Kazumori, Kevin Garrett, and Eric Maddy

49 Precipitation Ensemble Data Assimilation in NWP Models 983
 Takemasa Miyoshi, Shunji Kotsuki, Koji Terasaki, Shigenori Otsuka, Guo-Yuan Lien, Hisashi Yashiro, Hirofumi Tomita, Masaki Satoh, and Eugenia Kalnay

50 PERSIANN-CDR for Hydrology and Hydro-climatic Applications 993
 Phu Nguyen, Hamed Ashouri, Mohammed Ombadi, Negin Hayatbini, Kuo-Lin Hsu, and Soroosh Sorooshian

51 Soil Moisture and Precipitation: The SM2RAIN Algorithm for Rainfall Retrieval from Satellite Soil Moisture 1013
 Luca Ciabatta, Stefania Camici, Christian Massari, Paolo Filippucci, Sebastian Hahn, Wolfgang Wagner, and Luca Brocca

52 Drought Risk Management Using Satellite-Based Rainfall Estimates 1029
 Elena Tarnavsky and Rogerio Bonifacio

53 Two Decades of Urban Hydroclimatological Studies Have Yielded Discovery and Societal Benefits 1055
 J. Marshall Shepherd, Steven J. Burian, Menglin Jin, Chuntao Liu, and Bradford Johnson

54 Validation of Climate Models 1073
 Francisco J. Tapiador

55 Extreme Precipitation in the Himalayan Landslide Hotspot 1087
 Thomas Stanley, Dalia B. Kirschbaum, Salvatore Pascale, and Sarah Kapnick

56 The Value of Satellite Rainfall Estimates in Agriculture and Food Security 1113
 Tufa Dinku

**57 Using Satellite Estimates of Precipitation for Fire
Danger Rating** 1131
Robert D. Field

58 Variability of Satellite Sea Surface Salinity Under Rainfall 1155
Alexandre Supply, Jacqueline Boutin, Gilles Reverdin,
Jean-Luc Vergely, and Hugo Bellenger

List of Figures

Fig. 1.1 Schematic of the Global Precipitation Measurement (GPM) mission Core Observatory (CO; left) and the GPM international partner constellation (right). Note that as of 21 May 2018 the KaPR swath width has been increased to 245 km to match that of the KuPR. (Note that the GPM-CO alternates flight directions to keep the canted solar panel towards the Sun: half the time the flight direction is 180° from that shown) 5

Fig. 1.2 An infrared image from Himawari 8 of the “lake effect” clouds over the Japan Sea (top), and three-dimensional snapshot of shallow precipitation from those clouds observed by the effective radar reflectivity at Ku band of the GPM/DPR at 0955 UTC 2 December 2014 (bottom) 7

Fig. 1.3 Hail detection in the thunderstorm near Fort Worth, Texas, on 26 May 2015. (a) Hydrometeor identification by a ground-based polarimetric radar and (b) the output from the “flagHeavyIcePrecip” from the DPR product. (Adapted from Iguchi et al. 2018; see the reference for details) 8

Fig. 2.1 Highlights several of the unique features of the CloudSat data. The image shows an example of a tropical deep convective system with obvious heavy attenuation and multiple scattering effects. Attenuation can be so heavy at times that the surface reflection is not observed. The convective core area is identifiable through the lack of a radar bright band and elevated reflectivity maximum. Also notice the frequent detection of shallow isolated light showers with reflectivity generally <8 dBZ 27

Fig. 2.2 Panel (a) shows an estimate of effect of CloudSat fixed diurnal sampling on the annual mean Probability of Precipitation (PoP). The map shows the difference of the full CMORPH dataset from 2007 to 2010 from the CMORPH dataset subsampled at the CloudSat ground track. In most regions the effect causes an underestimate of the PoP that can be as large as 6%. Panel (b) shows an estimate of the effect of non-scanning sampling on the PoP again using CMORPH. The CMORPH data is restricted to the CloudSat sampling times at each latitude and compared to that calculated from a single cross section at a random longitude 28

Fig. 2.3 The fraction of total (rain & no-rain) pixels in which the surface signal is saturated by heavy attenuation 28

Fig. 2.4 The frequency of occurrence of surface precipitation of any phase. Occurrence is estimated using the certain precipitation flag in the 2C-Precip-Column product described below using data from 2007 to 2010 29

Fig. 2.5 The global frequency of occurrence of convective cores identified in CloudSat’s 2C-Precip-Column product using data from 2007 to 2010 31

Fig. 2.6 Variation of clear-sky surface backscatter with wind speed as derived from matched AMSR-E and CloudSat wind observations over the ocean, for a multi-month period and a fixed sea surface temperature range of 15 to 25 °C. Colors indicate normalized frequency of occurrence; the red line is the mean, and the dashed black lines are one standard deviation either side of the mean ... 34

Fig. 2.7 (panel a) the accumulate rainfall from the CloudSat 2C-Rain Profile product for the years 2007–2010; (panel b) the same from the DRP Ku band algorithm for a 2-year period from 2014 to 2016; (panel c) the difference between panels a and b; (panel d) the scatter plot of the rate difference shown in panel c with the saturation occurrence fraction from CloudSat 40

Fig. 3.1 Two-years times series of the flip maneuver schedule based on the beta solar angle (the angle between the sun direction and the orbital plan; see Capderou 2014 for details) 48

Fig. 3.2 Schematic of the effect of the relaxed control of the yaw 48

Fig. 3.3 Time series of maximum (red) and minimum (blue) latitude of the scan of the SAPHIR instrument 50

Fig. 3.4 Time series of the noise (NEΔT) for each channel of the SAPHIR sounder 51

Fig. 3.5 Zonal mean of the fraction of time for which the baseline product and the No-meghatropiques products differs by more than 50% of the daily accumulation. Summer 2012 conditions are considered. (Adapted from Roca et al. 2018) 52

Fig. 3.6 Brightness temperatures from SAPHIR channel 6 over the Tropical Atlantic on 6 September, 2017. The four scans correspond to consecutive orbits and show the developments of the two hurricanes IRMA and JOSE. These two hurricanes were observed within the same orbit, illustrating the unique feature of this observing system 54

Fig. 3.7 Fraction of SAPHIR observations per month which have been received and used a Météo-France before the cutoff times of the Météo-France global data assimilation system (4–5 h depending on the assimilation cycle) (Courtesy of Hervé Benichou, Météo-France DIROP/COMPAS/COM). The period starts in June 2015, which corresponds to the beginning of the operational assimilation of Megha-Tropiques data at Météo-France. The dashed red line refers to the averaged fraction over this 4-year period 56

Fig. 4.1 A time sequence of the microwave images of the super-typhoon NANGKA from 0540 to 1731 UTC 12 July 2015, superimposed on MTSAT IR images. (From NRL Tropical Cyclone page – <https://www.nrlmry.navy.mil/TC.html>, last accessed 21 Oct 2018) 64

Fig. 4.2 Scan geometries of the SSM/I sensors. (The COMET Program – <https://www.meted.ucar.edu/index.php>, last accessed 21 Oct. 2018) 68

Fig. 4.3 Scan geometries of the TRMM PR, TMI and VIRS. (Adapted from Kummerow et al. 1998) 69

Fig. 4.4 Scan geometries of the AMSU-A and AMSU-B sensors. (The COMET Program – <https://www.meted.ucar.edu/index.php>, last accessed 21 Oct 2018) 76

Fig. 5.1 MWI and ICI accommodation on Metop-SG 84

Fig. 6.1 State-of-the-art microwave monolithic integrated circuits low noise amplifiers’ noise figure 108

Fig. 6.2 A deployable reflector antenna concept for the small satellites. The antenna reflector surface can fit to less than 1.5 U volume and it is designed to operate up to ~100 GHz 108

Fig. 6.3 Roadmap of spaceborne precipitation radar 112

Fig. 7.1 Demonstrative atmospheric transmittances (total, H₂O and O₂) as a function of frequency and wavelength in the microwave region. (Adapted from Liou 2002, p. 415) 125

Fig. 7.2 Example of brightness temperatures as a function of column averaged rain rate at 19 GHz used to illustrate the “beamfilling” or non-homogeneous rain distribution effect 127

Fig. 8.1 Schematic for the GPROF Processing Algorithm. The three main components are the Sensor Profile Database, the Preprocessor, and the GPROF 2017 Processing Engine 143

Fig. 8.2 GPROF database distribution of Total Precipitable Water (TPW) and Two-Meter Temperature (T2M) profiles included in the a priori database year. These represent the number of database profiles in each TPW/T2 m and Surface Type category 146

Fig. 8.3 GPROF GMI retrieval of surface rain for hurricane Harvey, 25 August 2017 shortly before making landfall on the Texas coast. Over 60 inches (1500 mm) of precipitation was recorded near Houston over the next 5 days 149

Fig. 8.4 Solid (Snow) vs. Liquid Precipitation and Wet Bulb for both ocean and land locations. (Adapted from Sims and Liu 2015) 150

Fig. 8.5 GPROF zonal averaged precipitation retrieval for Total (left) and Frozen precipitation (right) for five GPM constellation sensors 151

Fig. 9.1 Schematic of MiRS processing components and data flow showing MiRS core retrieval and post-processing components. Core products are retrieved simultaneously as part of the state vector. Post-processing products are derived through vertical integration (water vapor, hydrometeors), catalogs (SIC, SWE), or fast regressions (rain rate). Post-processed hydrometeor retrieval products are indicated in red: Rain Rate, Graupel Water Path, Rain Water Path and Cloud Liquid Water 155

Fig. 9.2 Example of rain water (left) and graupel water (right) retrieval evolution for a single vertical profile based on NOAA-18 AMSU-MHS measurements. Top panels show rain and graupel water profile retrieval as function of iteration (3 iterations total). The remaining panels show the CRTM Jacobians with respect to rain and graupel at channels 15, 17, 18, 19, 20 (89, 157, 183 ± 1 , 183 ± 3 , and 190 GHz), for each iteration. In this case, the retrieval converged in 3 iterations. Rain and graupel particle effective radii were assumed to be 500 microns 159

Fig. 9.3 Comparison of global rain rate maps on 21 June 2016 from MiRS when applied to GPM/GMI (left) and SNPP/ATMS measurements (right). Examples of weather systems detected by both satellites are circled 160

Fig. 9.4 MiRS retrievals of hydrometeor and temperature structure around Typhoon Soudelor from Suomi-NPP/ATMS valid 0445 UTC on 6 August 2015. Panels show surface rain rate (top left), rain water 0.01 mm isosurface with temperature profile superimposed (top right), graupel water 0.05 mm isosurface with temperature profile superimposed (bottom left), and a vertical cross-section along 21°N of both rain and graupel water (bottom right) 161

Fig. 9.5 Comparison of MiRS SNPP/ATMS instantaneous rain rate (mm/h) (top) with operational NWS Stage IV rain rate (bottom) over the conterminous US for two different dates, 16 March 2016 (left), and 28 July 2016 (right) 162

Fig. 9.6 Example of impact of using retrieved CLW over land in the land precipitation estimation from SNPP/ATMS on 01 May 2016. Shown are (a) MiRS operational rain rate (mm/h), (b) MiRS rain rate using CLW, (c) MRMS Q3 radar-gauge analysis valid at 1900 UTC (units in inches), (d) MiRS Liquid Water Path (LWP = RWP + CLW, mm), and (e) visible satellite image from GOES-East valid at 1915 UTC 164

Fig. 9.7 Probability distribution functions of MIRS ATMS vs. Stage IV baseline (operational, no CLW included in rain rate estimation) and experimental rain rate (CLW included) over land during September–November 2016. Note improved frequency distribution and agreement with Stage IV in experimental rain rate. Distributions are for all points with Stage IV rain rate greater than 0 mm h⁻¹ 165

Fig. 11.1 DPR’s scan pattern before May 21 2018 (left) and after May 21 2018 (right). KaHS beams scan in the inner swath before May 21 2018, but now they scan in the outer swath and match with KuPR’s beams. Numbers in color indicate angle bin numbers for KuPR (blue), KaMS (yellow), and KaHS (red) 184

Fig. 11.2 DPR L2 algorithm flow 186

Fig. 12.1 Schematic plot of DFR_m profile with key points A, B, C, and D. Point A: slope of DFR_m has peak value. Point B: local maximum of DFR_m. Point C: local minimum of DFR_m. Point D: DFR_m value near surface 194

Fig. 12.2 Histogram of DFR_m index V3 and CDFs (cumulative density function) using total of 121,859 vertical profiles from GPM real data. (a) Histogram and 1-CDF of V3 for Stratiform rain. Red dashed line represents 1-CDF. (b) Histogram and CDF of V3 for Convective rain. Red dashed line represents CDF 196

Fig. 12.3 Block diagram of precipitation type classification model 197

Fig. 12.4 Block diagram of melting layer detection for DFR_m method 198

| | | |
|------------|---|-----|
| Fig. 12.5 | Left column (from top to bottom): comparison of melting layer top height (in km) between dual-frequency classification method and Ku only method for cyclone, hurricane and typhoons shown in Table 12.2. Right column illustrates similar results for melting layer bottom height (in km) | 200 |
| Fig. 12.6 | (a) GPM DPR overpass of rainfall rate on March 17, 2014 (#000272). Circled A, B and C represents snow, stratiform rain, and convective rain. (b) Averaged reflectivity profiles as well as dual-frequency ratio profile for snow. (c) Same as (b) for stratiform rain. (d) Same as (b) for convective rain | 202 |
| Fig. 12.7 | Vertical cross section at nadir of DPR overpass shown in Fig. 12.6a | 203 |
| Fig. 12.8 | GPM DPR overpass of rainfall rate on March 17, 2014. Scan # from 4894 to 5142. (a) Histogram of mean DFR_m slope in absolute value. (b) Histogram of maximum reflectivity at Ku band. (c) Histogram of storm top height | 204 |
| Fig. 12.9 | Large scale study of the snow index using GPM DPR profiles. Histograms of the snow index are shown for rain (blue) and snow (red). The blue dashed curve is the cumulative density function (CDF) for rain. The red dashed curve is 1-CDF for snow | 205 |
| Fig. 12.10 | Flowchart to perform surface snowfall identification in profile classification module of GPM DPR level 2 algorithm | 206 |
| Fig. 12.11 | Match ratio for 16 validation cases during the years 2014–2018 | 208 |
| Fig. 13.1 | CloudSat and GPM coincident overpass observations of a convective precipitation system developed over the Banda Sea in the Maluku Islands of Indonesia. Measurements from a suite of microwave sensors are shown. Top row: CloudSat W-band reflectivity; second row: GPM Ka-band reflectivities for the high sensitivity (HS) scan; third row: GPM Ku-band reflectivity for the normal scan (NS). The dataset of coincident overpasses is from the GPM product 2B-CSATGPM from the NASA Precipitation Processing System developed by J. Turk, JPL | 213 |
| Fig. 13.2 | Left: effective DFR_{Ka-W} vs DFR_{Ku-Ka} for population of raindrops at 15 °C with Γ DSDs with different m as indicated in the legend and with color-coded mean mass-weighted diameter. Right: extinction coefficient vs rain rate for exponential DSDs with intercept parameters as indicated in the legend. Scattering properties are computed using T-matrix | 216 |
| Fig. 13.3 | Effective DFR_{Ka-W} vs DFR_{Ku-Ka} for population of ice crystals computed different scattering tables. The density plots show the distribution measured by a triple-frequency radar during one of the GPM field campaigns | 218 |

Fig. 13.4 Left: gas-corrected Ka-band reflectivity (top), DFR_{Ku-Ka} (center) and DFR_{Ka-W} (bottom) for a flight on the 1 December 2016. Right top: flight tracks across the Olympic Peninsula from the Olympic Mountains range toward and beyond the NPOL radar (black dot) on the Pacific coastline. The UTC time of DC-8 (external contour) and Citation (internal contour) aircraft paths are modulated in color (see color bar). The position of the Citation is shown in the top left panel. Right bottom: hydrometeor classification according to the multi-frequency method of Tridon et al. (2019) 220

Fig. 13.5 Retrieved parameters for the leg shown in Fig. 13.4: mean mass-weighted maximum size (top), IWC (center) and flux (bottom). The right bottom panel shows the bulk ice density as defined in Leinonen et al. (2018) 221

Fig. 13.6 Comparison between in-situ and retrieved microphysical properties as sample by the Citation aircraft in the ice part corresponding to the upper leg as shown in Fig. 13.4. Left column: mean mass weighted particle size (top) and ice water content (bottom) for the in-situ and for the two retrievals considered in this paper. The blue lines and the blue bands correspond to the a-priori and its standard deviation. Right panel: scatterplot of IWC vs D_m for the in-situ and for the two retrievals. Note that the in-situ D_m and IWC are derived from the PSD measurements based on the assumption that the mass-size follows that of lightly rimed B-model of Leinonen and Szyrmer (2015) 222

Fig. 13.7 Shift of the retrieved particle size distributions towards lower sizes. Figure prepared by L. Pfizenmaier (see Pfizenmaier et al. 2019 for details) 224

Fig. 14.1 Illustration of two possible strategies to mitigate the large mismatches between the radar and radiometer footprint sizes in satellite combined retrievals 234

Fig. 14.2 (Left) Example of combined surface precipitation estimates for GPM orbit 605 on 1 October 2014. (Right) The associated Multi-Radar/Multi-Sensor (MRMS) estimates 238

Fig. 14.3 Density scatterplot of GPM combined V06 vs reference MRMS convective precipitation ($mm\ h^{-1}$) at the footprint scale over the period April 2014–October 2014 239

Fig. 14.4 (Left) Example of liquid water path (LWP) derived from GMI observations over oceans for orbit 003351 on 1 October 2014. (Right) The associated combined surface precipitation. The magnitude of the LWP suggests that light precipitation is undetected by the DPR 240

Fig. 14.5 (Left) Example of Ku-band PIA derived by the combined algorithm for orbit 003539 on 13 October 2014. (Right) The associated Ku-band PIA estimated exclusively from GMI observations 242

Fig. 14.6 (Left) Ku-band PIA derived by the combined algorithm for orbit 003351 on 1 October 2014. (Right) The associated Ku-band PIA derived from GMI brightness temperatures using the extended formulation described in the text 244

Fig. 15.1 Extinction (left) and backscattering (right) cross sections for spheres (continuous lines), perfectly oriented spheroids (dashed) and Rayleigh spheres (dotted) for single raindrops at 9.6 (red), 35.5 (green) and 94 (blue) GHz 260

Fig. 15.2 Reflectivity per unit mass for an exponential drop size distribution vs mean mass-weighted equi-volume diameter for spheres (continuous lines), perfectly oriented spheroids (dashed) at 9.6 (red), 35.5 (green) and 94 (blue) GHz 260

Fig. 15.3 Backscattering (Q_{bk} , left) and extinction (Q_{ext} , right) efficiencies defined as $Q = \sigma / \pi r_{eff}^2$ with r_{eff} being the radius of the equal mass ice sphere and σ the corresponding cross section. The size parameter x combines the dependence of the scattering variables on particle mass and wavelength. Spheroid approximations include spheres of solid ice (continuous black line), spheres with an ice-air mixture (black long-dashed) representing the mass-size relation of Brown and Francis (1995), and spheroids with the same mass-size relation but with and aspect ratio of 0.6 (black dotted). Scattering properties for unrimed (gray dots) and rimed (black dots) calculated with DDA in Leinonen and Szyrmer (2015) (results shown are for particle model B and the second most rimed particles). The SSRGA (gray solid line) has been derived for the same ensemble of unrimed aggregates (Leinonen et al. 2018a, b). The vertical lines denote the size parameter for X, Ka and W Band assuming a particle mass of 10 mg which corresponds for example for the unrimed aggregates to a maximum snowflake size of 3 cm 263

Fig. 15.4 Extinction (left) and backscattering (right) cross sections for partially melted snow aggregates at 10% (dark) and 50% (gray) melted fractions. Results are from DDA scattering simulations (Ori et al. 2014) at 9.6 (continuous), 35.5 (dashed) and 94 (dash-dotted) GHz 269

Fig. 16.1 The spread of Z-S relations under different assumptions of particle shapes. (Adapted from Hiley et al. 2011) 280

Fig. 16.2 Z-S relation for three nonspherical snowflakes. A least square fitting curve and relation by Matrosov (2007) are also shown. (Adapted from Liu 2008b) 281

Fig. 16.3 Scatterplot of coincident CloudSat CPR and GPM/DPR Ku-band reflectivities for snowing cases. Data in the green box are those above the minimum detection for both Ku and CPR radars 282

Fig. 16.4 PDFs and cumulative PDFs of snowfall occurrence and snowfall rate derived by coincident CPR and DPR observations using Z-S relations as discussed in the text. Data period for these plots is from March 2014 to December 2015 283

Fig. 16.5 CloudSat CPR radar reflectivity for 2 snowfall cases on 21 August 2007 (top) and 17 July 2006 (bottom) over 50–60°S. The top case is associated with deep snowing clouds cross a frontal system and the bottom case is associated with very shallow snowing cloud cells next to moderate deep snowing clouds 284

Fig. 16.6 Frequency of total precipitation (rain and snow, left), frequency of snowfall (middle) and mean snowfall rate (right) for northern (top) and southern (bottom) hemispheres derived from CloudSat observations from July 2006 to June 2008. The diagrams cover the area from the Poles to 40°N/S. Detailed descriptions of the retrieval method can be found in Liu (2008b) 285

Fig. 16.7 Zonally averaged frequency of occurrence of rainfall (blue), frequency of snowfall (gray, stacked above blue) and snowfall rate (red). Derived using CPR –15 dBZ as precipitation threshold, rain-snow separation scheme of Sims and Liu (2015), and Z-S relation of Liu (2008b) 286

Fig. 16.8 Number and volume frequency distributions of snowfall rate derived from CloudSat observations. Note the frequencies are calculated in a snowfall rate interval on logarithm scale 286

Fig. 16.9 Mean profiles for a given near surface snowfall rate for (a) over ocean and (b) over land environments. CloudSat observations from July 2006 to June 2007 are used. (Adapted from Liu 2008b) 287

Fig. 16.10 Relation between near surface snowfall rate and cloud top height as expressed by snowfall profiles frequency distributions for snowfall events over (a) ocean and (b) land. The frequency values are normalized so that the maximum frequency is 100. (Adapted from Liu 2008b) 288

Fig. 16.11 Mean liquid water path as a function of cloud top temperature and near surface radar reflectivity for different snowing cloud types: (a) Isolated shallow clouds, (b) Isolated deep clouds, (c) extended shallow clouds, and (d) Extended deep clouds. Coincident CloudSat CPR and Aqua AMSR-E observations from June 2006 to June 2010 are used. Note that the LWP color scales for isolated and extended clouds are different. (Adapted from Wang et al. 2013) 289

Fig. 16.12 Mean snowfall rate maps derived from multiple years of CloudSat (2007–2010), GMI (March 2014–Feb 2018), and MHS (2007–2010). GMI algorithm is trained by combined CloudSat and DPR radar data. No observations in blank areas. MHS algorithm is trained by CloudSat CPR 291

Fig. 17.1 CloudSat derived ice water content (IWC) profiles. The values have been normalized 306

Fig. 17.2 Stage IV vs. S-NPP SFR scatter plot from (a) before calibration, and (b) after calibration 307

Fig. 17.3 PDFs of S-NPP SFR and Stage IV (a) before, and (b) after calibration 308

Fig. 17.4 S-NPP ATMS SFR using (a) satellite-only SD algorithm, and (b) hybrid SD algorithm during a major snowfall event on 5 February 2014 in the US Image (c) is the near coincident radar reflectivity which covers both snowfall and rainfall (in the southern part of CONUS). The noted oval areas in (a) and (b) show legitimate snowfall that was missed by the satellite-only algorithm but captured by the hybrid algorithm 309

Fig. 17.5 (a) Scatter plot of Stage IV vs. collocated S-NPP SFR validation data, and (b) PDFs of the same data sets 310

Fig. 17.6 Comparison of (a) S-NPP SFR 3-month average from January - March 2017 and (b) the corresponding Stage IV data 310

Fig. 18.1 (Lower left image) Synoptic view of Hurricane Gustav over south eastern Louisiana on September 2, 2008 12:00 UTC taken from NEXRAD weather radar reflectivity mosaic. The white box shows an outer rain band around 30.5° N × 89.5° W. (Central image) Geographic representation of the NEXRAD image at 0.86° elevation, acquired by the S-band radar (KMOB, in figure) near Mobile (Alabama). The semi-transparent rectangular box represents the scene of interest, acquired by TSX X-SAR on 2 September 2008 12:00 UTC in HH polarization and ScanSAR mode (100 km swath). (Upper right image) TSX quicklook of the acquisition in arbitrary units at 100-m resolution; flight direction is indicated. (Adapted from Marzano et al. 2010) 319

Fig. 18.2 Correlation diagram between NRCS values X-band σ_{SAR} against co-located and co-registered S-band NEXRAD weather-radar reflectivity Z , for a selected region of interest (ROI) of the scene. The upper axis provides the estimated rain-rate from NEXRAD data using the Marshall-Palmer relation (Bringi and Chandrasekar 2001). The best-fitting curve is also plotted. (Adapted from Marzano et al. 2010) 320

Fig. 18.3 TRMM observations, at 15:30 UTC, for the case study of Hurricane Gustav. (Top panels) TRMM 1B11 brightness temperature (TB) product relative to TMI channel 7 (37 GHz horizontal polarization, left), beam effective field-of-view (EFOV) of $16 \times 9 \text{ km}^2$, and TMI channel 9 (85.5 GHz horizontal polarization, right) with a main-beam EFOV of $7 \times 5 \text{ km}^2$. The cyclonic cell indicated in Fig. 18.2 is well captured. (Bottom panels) The TRMM 1C21 radar reflectivity (dBZ) product, relative to PR normal sample (left) range bin 75, and PR rain oversample (right), range bin 16. Note that the PR swath is 220 km wide (reduced in the oversampled product) and the range resolution is 0.25 km; TMI swath is 760 km wide. (Adapted from Marzano et al. 2011) 321

Fig. 18.4 Schematic SAR NRCS (in dB) as a function of cross-track scanning distance x , showing enhanced values on the left of the cross-over point caused by scattering from the cloud top and attenuation from rain in the lower cloud on the right. The viewing angle with respect to nadir (incidence angle) is θ , while the cloud extension is w . The symbol Δr indicates the width of the slant slice of the atmosphere representing the SAR side-looking resolution volume. The figure also shows the energy fluxes and the e.m. parameters of the model according to Marzano et al. (2012) and Mori et al. (2017a) 323

Fig. 18.5 Example of System for Atmospheric Model (SAM) vertical slice for a Compact Medium Single Cell cloud. Values indicate water content W in g m^{-3} of the simulated distributions of snow, rain, ice and cloud particles 326

Fig. 18.6 SAR simulated response in terms of normalized Radar cross section σ_{SARhh} (horizontal transmitted and received), co-polar ratio Z_{SARco} and complex correlation coefficient ρ_{SARco} for the SAM realistic cell of Fig. 18.5. Four SAR frequencies evaluated (5.4, 9, 14 and 35 GHz). Considered background are Spheres, Dihedrals, Cylinders, and a semi-empirical bare soil (SEM) 327

Fig. 18.7 Flowchart of the procedure described in Mori et al. (2016) for detecting flooded and cloud areas in X-SAR images and estimating the relative precipitation rate 332

| | | |
|------------|---|-----|
| Fig. 18.8 | Voghera case study. Left image is a geocoded quicklook of the CSK acquisition (at 05:18 UTC). Right figure shows the corresponding Italian National Mosaic Vertical Maximum Intensities (VMI) at 05:30 UTC (~15 min acquisition time); the ellipse approximately encloses the case study area. (Adapted from Mori et al. 2017b) | 334 |
| Fig. 18.9 | Precipitation maps for the case study of Fig. 18.8. Left map is obtained from X-SAR data with the procedure of Sect. 18.5.1 (filtered and smoothed to WR resolution), right map is obtained by WR VMI data and a Marshall-Palmer formula. (Adapted from Mori et al. 2017b) | 334 |
| Fig. 18.10 | Right plot shows the analysis of the position error between the WR precipitation map (shaded background) and the SAR one (foreground) for the case study of Fig. 18.8. Values have been normalized to the maximum of the dataset. Note that the WR data precedes the SAR data by ~12 min. Left plot shows Complementary Cumulative Distribution Function (CCDF) for the same case study. Blue lines represent SAR data degraded at WR resolution (1000 m); red lines represent WR data. (Adapted from Mori et al. 2017b) | 335 |
| Fig. 19.1 | PMW sensor Equator-crossing times for 12-24 Local Time (LT; 0000-1200 LT is the same) for the modern PMW sensor era. These are all ascending passes, except F08 is descending. Shading indicates that the precessing TRMM, Megha-Tropiques, and GPM cover all times of day with changes that are too rapid to depict at this scale. (Image by Eric Nelkin (SSAI; GSFC), 12 July 2018; https://pmm.nasa.gov/sites/default/files/imce/times_allsat.jpg holds the current version, last accessed 1 Apr. 2019) | 345 |
| Fig. 19.2 | Rainfall accumulations for the week of 25-31 August 2017 over the US Gulf Coast for NOAA Multi-Radar Multi-Sensor (MRMS) data (left) and IMERG V05 Late estimates (right). Houston, Texas is just west of Area 1 | 350 |
| Fig. 19.3 | Time series of area-average rainfall for the week of 25-31 August 2017 over the US Gulf Coast for the near-coastal Area 1 (top) and the more inland Area 2 (bottom). Houston, Texas is just west of Area 1. The IMERG Late averages are labeled precipitationCal, and the IR-based precipitation time series is IRprecipitation | 351 |
| Fig. 20.1 | Image of “JAXA Global Rainfall Watch” website (http://sharaku.eorc.jaxa.jp/GSMaP/ , last accessed 15 Oct. 2018) | 357 |
| Fig. 20.2 | Process flowchart for the GSMaP product | 359 |
| Fig. 20.3 | Distribution of the daily rain amount around Japan on June 25, 2017 for (a) JMA radar-AMeDAS, (b) GC V6, (c) MVK V6, (d) NRT V6, (e) NOW V6, and (f) Hydro-Estimator (H-E) | 365 |